Journal of High School Science

Engineering cerium oxide nanoparticles for tunable wettability properties

Kumaraswamy T[1], Sachith M.V[2], Sastry O[3], Karthik N[4], Swetha N[5], Ramya Prabhu B[*5]

Submitted: March 19, 2025, Revised: version 1, June 14, 2025, version 2, July 18, 2025, version 3, August 12, 2025, version 4, August 13, 2025
Accepted: August 29, 2025

Abstract
The synthesis and design of nanomaterials with distinctive physical and chemical properties provides novel opportunities to utilize them in various applications. Nanomaterials' structures and surface characteristics significantly influence their physicochemical properties. These properties can be modified by tuning their synthesis reaction parameters. Here, we provide a simple and effective wet chemical method for the controlled synthesis of cerium oxide nanoparticles (CeO_2 NPs) functionalized with citric acid or Cetrimonium bromide (CTAB) as the capping agents. The synthesized CeO_2 NPs were characterized using XRD, Raman spectroscopy, FESEM, TEM, and FTIR to study the crystal structure, morphology, and functional groups. The CeO_2-capping agent molecules were found to be arranged in a crystalline cubic lattice in the nanoparticles. We investigated the surface wettability for various functionalized CeO_2 NPs by contact angle measurements. We found that the morphology and hydrophobicity of the NPs could be changed by changing the capping agent. The functionalization of CeO_2 with CTAB resulted in maximum enhancement in the hydrophobicity with a contact angle of 92.2 ± 3.3°. This work provides valuable insights into surface functionalization of CeO_2 NPs as a method to modulate their morphology and wetting characteristics.

Keywords
Cerium oxide nanoparticles, Capping agent, Cetrimonium bromide, Citric acid, Nanoparticle functionalization, Surface wettability, Nanomaterials, Hydrothermal synthesis, Morphology, Hydrophobicity

[1]Tanesha Kumaraswamy, Vijaya Bharathi PU College, Bengaluru, Karnataka, India. taneshak1234@gmail.com
[2]Sachith Mahantesh Veerapur, Rashtrotthana Vidya Kendra, Banashankari, 6th Stage -7th Block, Bengaluru, Karnataka 560060, India. jh19121979@gmail.com
[3]Ojaswin Sastry, Purnapramati School, 26/1, 1st Cross, Hoskerehalli Main Road, Girinagara, Bengaluru, Karnataka 560085, India. ojaswin.sastry@gmail.com
[4]Karthik Nagendra, Sai Krushna Vidya Mandir, Hosadoddi Village, Off Kanakapura Road, Bolare, Post, Bengaluru, Karnataka 560082, India. rn1580256@gmail.com
[5] Swetha Nataraj, Prayoga Institute of Education Research, Kanakapura Rd, off, Ravgodlu, Post, Bengaluru, Karnataka 560082, India. swetha.n@prayoga.org.in
[5*]Corresponding author: Ramya Prabhu Bantwal, Prayoga Institute of Education Research, Kanakapura Rd, off, Ravgodlu, Post, Bengaluru, Karnataka 560082, India. ramyaprabhu.b@gmail.com

https://doi.org/10.64336/001c.144173

Introduction

The synthesis of metal oxides of a particular shape, size, and dimension has attracted considerable interest among researchers (1-3). Among these rare earth metal oxides, cerium oxide nanoparticles (CeO_2 NPs), in particular have garnered significant attention due to their tunable physicochemical properties and acceptable biocompatibility (4,5). The properties of these nanoparticles are useful in applications relating to oxygen storage capacity, redox activity, catalytic efficiency, energy storage, biomedical devices and environmental remediation (6,7). The synthesis of CeO_2 NPs with controlled size, morphology, and surface properties is critical for optimizing their performance in these applications.

Researchers have employed various methods, including sol–gel, hydrothermal, and precipitation techniques, to synthesize CeO_2 NPs, each offering distinct advantages regarding particle size distribution and surface chemistry. (8,9). One of the key surface properties of CeO_2 NPs is their wettability, which plays a crucial role in determining their interaction with liquids and other materials. Wettability, characterized by the contact angle of a liquid droplet on a solid surface, is influenced by surface roughness, chemical composition, and surface energy (10). These hydrophobic surfaces play a vital role in present-day applications such as in the production of water-resistant textiles and self-cleaning glass; among others. Hydrophobic coatings protect metal surfaces from corrosion and increases their durability (11,12). Hydrophobic surfaces also play a significant role in developing self-cleaning and anti-fouling technologies. CeO_2 NPs are applied in coatings, sensors, and self-cleaning surfaces, where controlled liquid–solid interactions are required. The wettability of CeO_2 NPs can be tuned by modifying their surface chemistry, which alters their surface energy and morphology.

Mai et al. proposed a synthesis method to form CeO_2 NPs. They reacted cerium nitrate and sodium hydroxide hydrothermally at 180 °C. By changing NaOH concentration and hydrothermal reaction temperatures, they could change the morphology of the resultant CeO_2 NPs (13). Li et al. synthesized superhydrophobic CeO_2 nanotubes with a contact angle of 157°, which exhibited excellent resistance to greasy contaminants, long-term durability in chemical environments, and extraordinary thermal stability even at temperatures as high as 450 °C (14). Rare earth metals exhibit hydrophobicity because their unique electronic structure prevents the formation of hydrogen bonds with water molecules (15). Sanders et al. synthesized functionalized CeO_2 NPs by grafting aryl groups on their surface. They found that hydrophobicity increased with alkyl chain length and achieved a 124.9° ± 6.9° contact angle for 4-n-butylbenzene diazonium grafted CeO_2 NPs (16). Despite these advances, a comprehensive understanding of the relationship between synthesis parameters, surface properties, and the wettability of CeO_2 NPs has eluded explanation and remains an area of active research.

In this study, we synthesized CeO_2 NPs using a facile hydrothermal method employing various capping agents and investigated the physicochemical properties of the formed NPs. Further, we measured the contact angle of these NPs to study their wetting properties. The synthesis of unique morphological CeO_2 with functional groups is beneficial for

designing hydrophobic surfaces. We demonstrated the dual role of capping agents in achieving the desired morphology and the enhanced hydrophobicity.

Materials and Methods

$Ce(NO_3)_3 \cdot 6H_2O$ (99%) was from Sigma Aldrich. Citric acid, CTAB, NaOH and commercial grade CeO_2 (99.9%) were from SRL Pvt. Ltd. (Mumbai, India), and HPLC-grade ethanol from Spectrochem Pvt. Ltd. (Mumbai, India). We used distilled water for the reaction and Type 1 water for the dialysis and the zeta potential experiments. All chemicals were used as received, without further purification.

The hydrothermal reaction was performed in a Teflon-lined autoclave consisting of a 50 mL Teflon chamber housed within a high-quality, threaded stainless steel outer jacket. (AK Engineering, Bengaluru, India). Samples were dried in a hot air oven (UTC 221P multispan, also from AK Engineering, Bengaluru, India). A Supertek refrigerated centrifuge (Supertek Scientific, Addison, IL) was used to separate the nanoparticles from the solution.

We characterized the surface morphologies of the synthesized CeO_2 nanostructures using a TESCAN MIRA3 LM field emission scanning electron microscope (FESEM, Czech Republic). We dispersed the samples in ethanol, drop-cast them onto silicon substrates (0.5 × 0.5 cm^2), and dried them under vacuum overnight. We determined the nanostructures' crystal structure and phase composition using a Rigaku SmartLab X-ray diffractometer (XRD, Rigaku Corp. Tokyo, JP) with Cu Kα radiation (λ = 1.5406 Å), operated at 40 kV and 30 mA. We uniformly dispersed a 500 mg portion of dried CeO_2 NP powder on a standard sample holder and flattened the surface using a glass slide. The instrument recorded the XRD pattern in the 2θ range of 10° to 90°, with a step size of 0.01° and a scanning rate of 1° min^{-1}. Measurements were repeated twice. We evaluated the synthesized material's bandgap by measuring the powder samples' diffuse reflectance with a PerkinElmer Lambda 750 spectrophotometer (Perkin-Elmer, Shelton, CT). We performed Raman spectroscopy on the synthesized CeO_2 powders using a Horiba Jobin Yvon-XploRa PLUS V2.1 multiline confocal Raman microscope (Horiba Corp. Kyoto, JP). We placed a 50 mg portion of the CeO_2 nanoparticle powder on a microscope slide for analysis. The spectra were recorded employing a 532 nm excitation wavelength and 2.5 mW laser power, focused through a 50X long-working-distance objective. The measurement parameters for the Raman spectra were an exposure time of 10 seconds and two accumulations. We performed transmission electron microscopy (TEM) analysis using a TALOS F200S G2 FEG microscope (Thermo Fisher Scientific, Waltham, MA) operating at 200 kV, equipped with a 4K × 4K CMOS camera and an in-column energy-dispersive X-ray (EDS) detector. For TEM sample preparation, the material was dispersed in ethanol (0.1 mg/mL) and sonicated in a bath sonicator for 10 minutes. Five µL of the solution was drop-cast onto a holey carbon-coated copper grid with 300 mesh (Ted Pella) and dried overnight in a vacuum desiccator. The particle size distribution was determined using ImageJ software. We measured the zeta potential of the CeO_2 NP dispersions (0.5 mg/mL) using an Anton Paar Litesizer™ 500 particle analyzer (Anton Paar, Ashland, VA), equipped with a 40-mW single-frequency laser diode (λ = 658 nm). The experiment

measured the zeta potential at a detection angle of 15° at room temperature. Each sample completed 100 sequential runs with a 30-second equilibration time between measurements. Thermogravimetric analysis (TGA) was performed using a Mettler TGA/DSC2 instrument (Metttler-Toledo, Colombus, OH) to determine the organic weight percentage in the CeO_2 samples. The sample was heated from 30 °C to 700 °C at 10 °C/min in a nitrogen atmosphere. The balance resolution was 0.1/1 µg, and the weighing accuracy was ± 0.005%. To measure the contact angle, all the samples were dispersed in ethanol (10 mg/1 mL) and sonicated for 10 minutes. A 500 µL portion of each solution was drop-cast on a 1 × 1 cm² glass substrate and heated at 50 °C for 5 minutes. We used this substrate for contact angle measurements. We analyzed the wetting properties of the drop-casted samples using a Contact Angle Meter (DM501, Kyowa Corp. Saitama, JP) by the sessile drop method using a 1 µL water drop for all the samples. The sessile drop method determined the contact angle of a probe liquid on a solid surface.

Synthesis of CeO_2 nanostructures

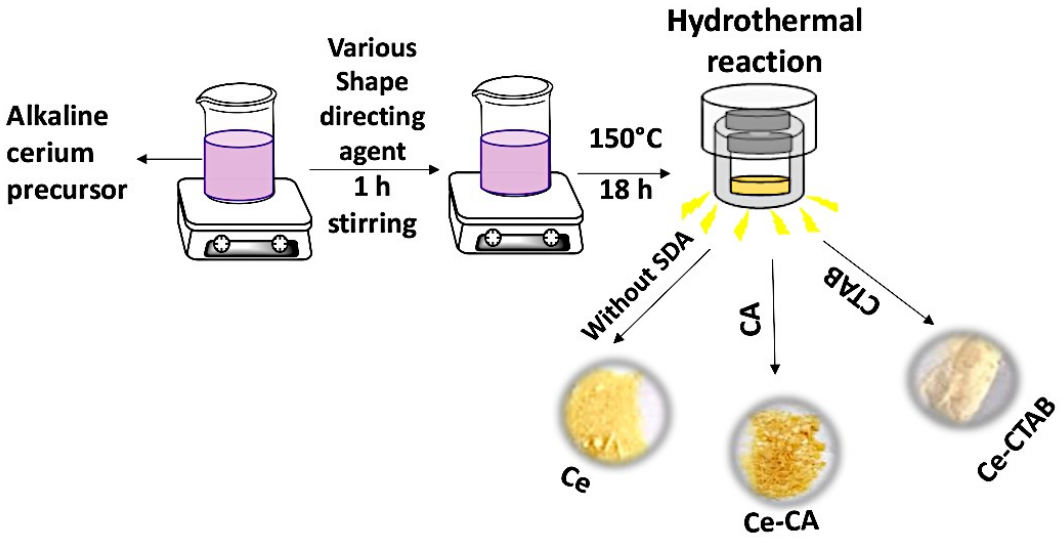

Figure 1. Schematic illustration of the synthesis procedure for the growth of CeO_2 nanostructures.

The capped CeO_2 nanoparticles were synthesized using a simple, one-pot hydrothermal method with 0.1 M cerium nitrate and 1 M sodium hydroxide as precursors, and 0.025 M citric acid (CA) and 0.025 M cetrimonium bromide (CTAB) as capping agents. The reaction proceeded at 150 °C for 18 hours. The powder obtained was washed with a 50:50 EtOH: water solution, centrifuged at 9558 g for 20 minutes, and then dried on a petri dish in a hot air oven at 80 °C for 4 hours. The product was stored in moisture-proof vials in a vacuum desiccator until analyzed for further characterization.

Dialysis of CeO_2 NP was performed to removed residual non-adsorbed capping agents. A 1 mg/mL dispersion of CeO_2 NP was prepared in Type 1 water. 20 mL of the

dispersion was loaded into a regenerated cellulose membrane dialysis tubing with a circular internal diameter of 22 mm, and a MWCO of 10,000 Da (Thermo Fisher). The dialysis was performed in one liter of Type 1 water for 72 hours at 300 rpm stirring at room temperature. We replaced dialyzate every 24 hours. After dialysis, the CeO_2 NP dispersion in the dialysis tubing was transferred to a centrifugation tube and centrifuged at 9558 g for 25 minutes to separate the CeO_2 NP. After decanting the supernatant, the CeO_2 powder was then dried in a hot air oven at 80°C for 4 hours and used for TGA analysis. Figure 1 shows the pictorial representation of the synthesis of the CeO_2 NP.

Results and discussion

Adding NaOH to the cerium nitrate solution formed a $Ce(OH)_3$ precipitate. A high pH provided by the NaOH oxidized the Ce^{3+} to Ce^{4+} (13,17). The hydrothermal conditions provided a conducive atmosphere to produce CeO_2 NP. Table 1 shows the nomenclature of the synthesized nanoparticles.

Table 1. CeO_2 NP nomemclature

Cerium nitrate (M)	NaOH (M)	Capping agent	Capping agent (M)	Nomenclature of obtained CeO_2 NP
0.1	1	None	-	*Ce*
0.1	1	Citric acid	0.025	*Ce-CA*
0.1	1	cetrimonium bromide	0.025	*Ce-CTAB*
Commercially procured		-	-	*Ce-Com*

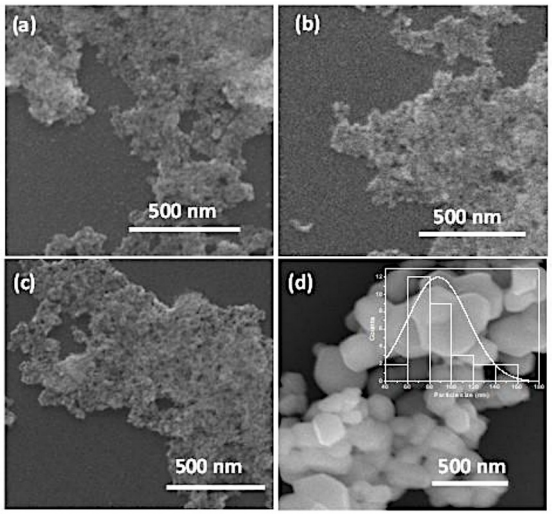

Figure 2. FESEM images of CeO_2 nanostructures **(a)** Ce **(b)** Ce-CA **(c)** Ce-CTAB **(d)** Ce-Com. The inset shows a histogram of particle size distribution.

Figure 2 shows the FESEM images of the CeO_2 nanostructures. The unfunctionalized CeO_2, particles are not distinctly visible 2(a). Their smaller particle sizes cannot be determined by FESEM imaging. Figures 2 (b,c) shows images of CeO_2 synthesized with

capping agents, captured at a magnification scale of 500 nm. In these images, the particles appear as clusters, making it challenging to determine their exact morphology. Therefore, a TEM analysis was performed to evaluate the morphology in detail. However, the commercial CeO_2 particles are clearly visible in the FESEM (Figure 2 (d)), and their size ranges from 40 nm to 160 nm (average: 88 nm). The histogram in Figure 2(d) inset shows their particle size distribution.

We performed an XRD analysis of Ce, Ce-CA, Ce-CTAB, and Ce-Com in an attempt to further decipher their crystal structure, as shown in Figure 3.

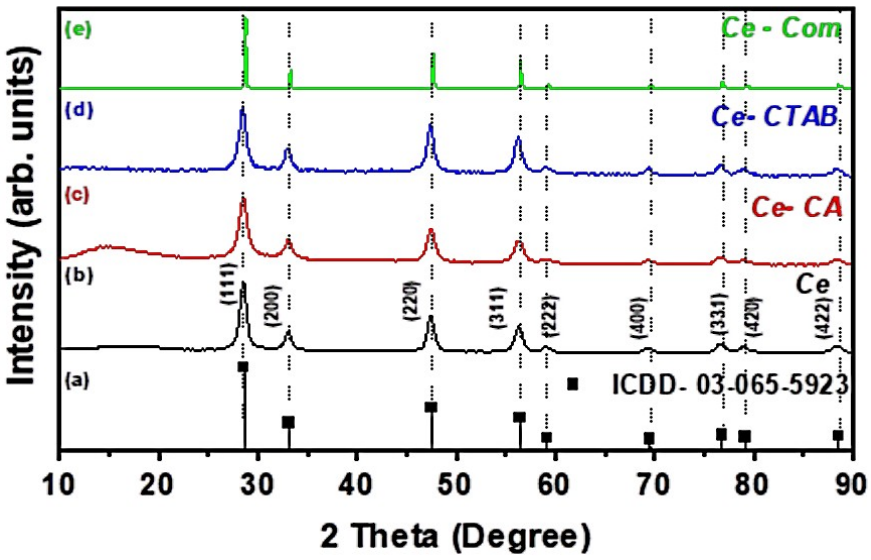

Figure 3. X-ray diffractogram of **(a)** standard spectra of cubic CeO_2 (JCPDS No. 03-065-5923) **(b)** Ce **(c)** Ce-CA **(d)** Ce-CTAB **(e)** Ce-Com.

All CeO_2 particles (b-e) consisted of 8 significant peaks corresponding to 28.5° (111), 33.0° (200), 47.5° (220), 56.4° (311), 59.3° (222), 69.3° (400), 76.7° (331), 79.2° (420) reflections. These reflections matched the cubic phase of CeO_2 ICDD No. 03-065-5923 (Figure 3 (a)). We observed that the XRD peaks of all the synthesized nanoparticles were broadened compared to the commercial CeO_2. NPs typically show peak broadening due to their reduced size and defects produced during the synthesis conditions. Additionally, lattice strain introduced during synthesis can further contribute to peak broadening (18).

The morphology, particle size, and crystallographic properties of the synthesized CeO_2 Nps were investigated using TEM. Figure 4 shows the TEM analysis of *Ce*. Figure 4(a) show CeO_2 NPs at low magnification; however, the size and morphology of the particles were not very clear. Figure 4 (b, c) shows the magnified image; the particle size was < 15 nm shaped in the form of irregular polygons. The histogram shows the *Ce* nanoparticles' size distribution (Figure 4 (d)) with a maximum ~ 9 nm. The interplanar spacing from the high-resolution TEM was 3.1Å, corresponding to (111) planes of cubic CeO_2. The lattice fringes were well defined and showed a high

degree of crystallinity. Figure 4 (e) shows Ce's selected area diffraction (SAED) pattern. The bright concentric ring in the SAED pattern confirms the polycrystalline nature of the *Ce*. The diffraction spots correspond to the (111), (200), (220), (311), (331), and (422) crystallographic planes. The X-ray diffraction also identified these planes.

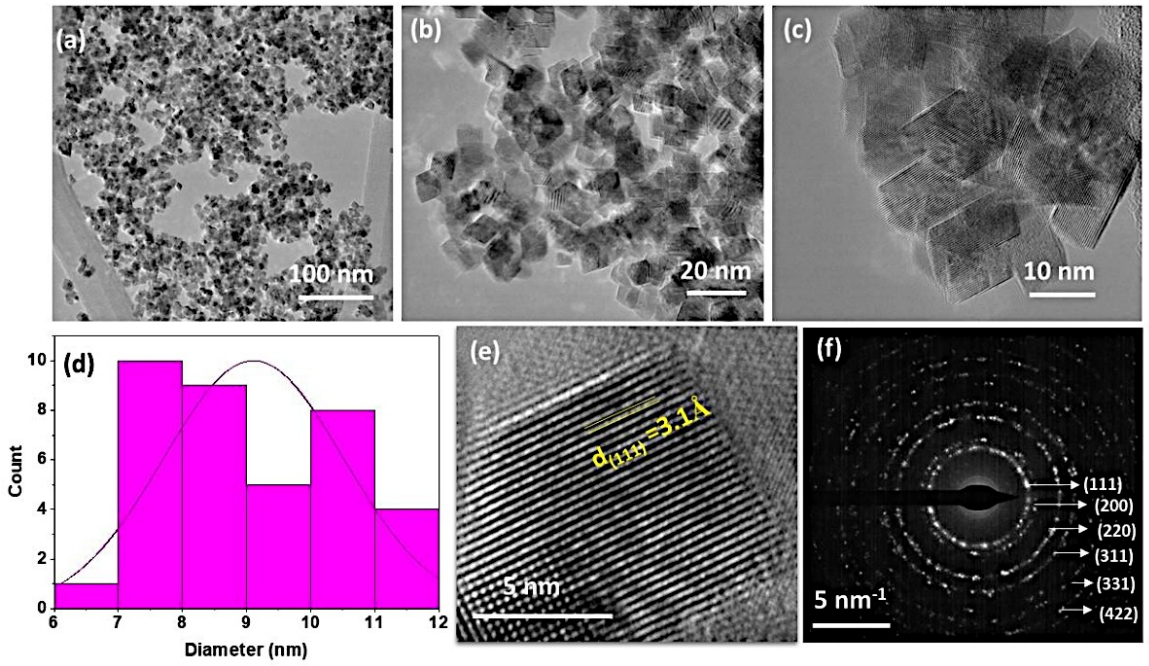

Figure 4. TEM images of Ce **(a)** Low magnification image **(b, c)** High magnification images **(d)** Histogram showing the size distribution of nanoparticles **(e)** HRTEM analysis **(f)** SAED analysis.

To investigate the influence of the capping agent on the morphology and structural properties of CeO_2 nanoparticles, we performed TEM analysis on CeO_2 NPs synthesized using citric acid as a capping agent (Figure 5). Figure 5(a) shows the resulting Nps at low magnification. At high magnification (Figures 5(b, c)), the morphology and size of the Ce-CA nanoparticles become increasingly distinct and well-defined. The CeO_2 NPs showed spherical morphology, consisting of an average particle size of ~7 nm (Figure 5(d)), demonstrating a reduction in size compared to unfunctionalized CeO_2 NPs (~ 9 nm). This reduction in size highlights the effectiveness of citric acid in modulating the growth and aggregation of the nanoparticles during synthesis, consistent with previous studies on the role of capping agents in nanoparticle synthesis (19,20).

The HRTEM analysis showed a clear lattice fringe with interplanar spacings of 1.9 Å corresponding to the (220) plane (Figure 5 (d)). The SAED pattern obtained from the nanoparticles exhibited well-defined diffraction rings, corresponding to the crystallographic planes (111), (200), (220), (311), (331), (400), (420), and (511), confirming the polycrystalline nature of the nanoparticles. The sharp and distinct diffraction spots within the rings further confirmed the nanoparticles' high crystallinity, which was consistent with

previous reports on polycrystalline CeO_2 NPs (21,22).

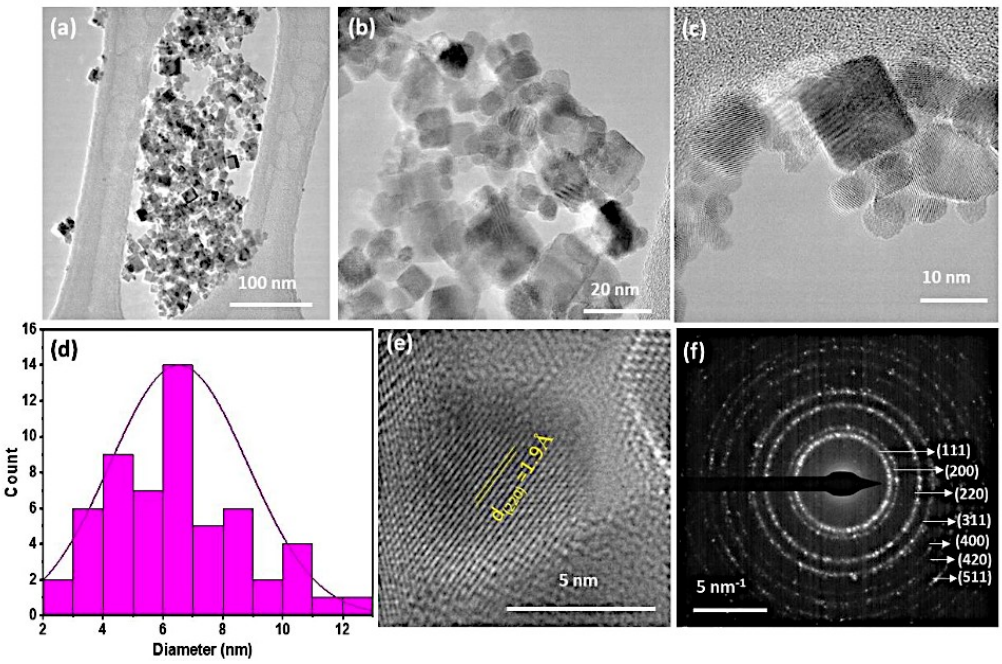

Figure 5. TEM images of Ce-CA **(a)** Low magnification image **(b, c)** High magnification images **(d)** Histogram showing the size distribution of nanoparticles **(e)** HRTEM analysis **(f)** SAED pattern.

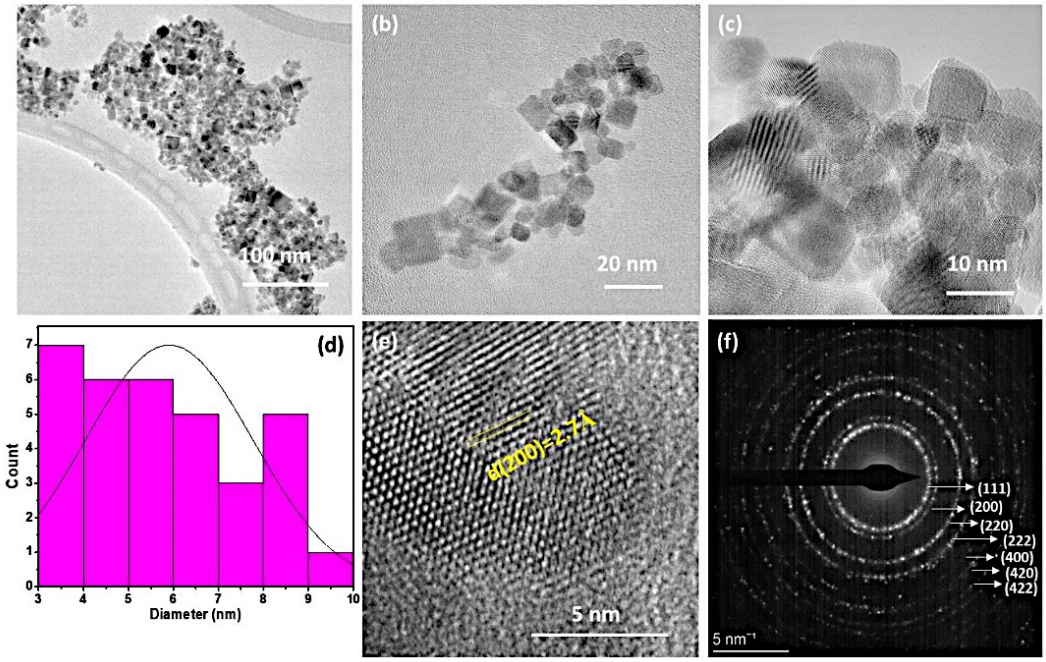

Figure 6. TEM images of Ce-CTAB **(a)** Low magnification image **(b, c)** High magnification images **(d)** Histogram showing the size distribution of nanoparticles **(e)** HRTEM **(f)** SAED pattern.

Figure 6 shows the effect of CTAB on the morphology and crystal structure of CeO_2 NPs. Figure 6 (a) shows the low-magnification image of *Ce-CTAB*. In Figure 6 (b, c), the spherical particles and irregular polygons can be seen. The average particle size of these NPs was ~ 6 nm, and Figure 6(d) presents the corresponding histogram. This indicated a reduction in the size of the *Ce-CTAB* compared to unfunctionalized CeO_2 NPs, which exhibited an average size of 9 nm. The analysis calculated the standard deviation (SD) by running a t-test for both samples, Ce-CTAB and Ce-CA. The SD for *Ce-CTAB* was 1.86, Ce-CA was 2.45, and the t-statistic was -3.71, with a corresponding p-value < 0.05, indicating that the particle size difference between these samples was statistically significant. The HRTEM imaging showed distinct lattice fringes with interplanar spacings corresponding to the (220) plane. The measured d-spacing of 2.7 Å for the (200) plane was consistent with the cubic structure of CeO_2, confirming the nanoparticles' high crystallinity and phase purity. The SAED pattern obtained from the nanoparticles showed well-defined diffraction rings (Figure 6(f)) that corresponded to the fluorite cubic structure of CeO_2. The observed rings corresponded to the crystallographic planes (111), (200), (220), (222), (400), (420), and (422), confirming the polycrystalline nature of the nanoparticles. These planes were consistent with the face-centered cubic (fcc) structure of CeO_2, as referenced in the standard crystallographic database (ICDD 03-065-5923).

Raman spectroscopy is a highly sensitive and non-destructive analytical technique for investigating metal oxide nanomaterials' structural, vibrational, and surface properties. We performed a Raman spectra analysis of all the synthesized NPs (Figure 7). A prominent peak was seen in all the samples ~ 462 cm^{-1}, confirming the formation of CeO_2. This F_{2g} band arises due to the symmetrical stretching vibration of the $Ce–O_8$ units (23). These vibrations were quite intense since Ce-O bonds are highly polarizable. Compared to the *Ce-Com,* all other synthesized CeO_2 NPs showed peak broadening due to the lattice distortion, consistent with the XRD results.

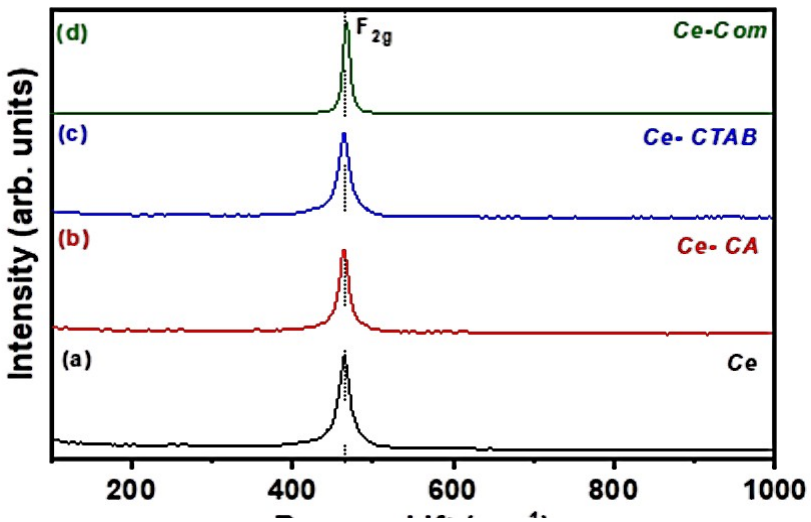

Figure 7. Raman spectra of CeO_2 nanostructures **(a)** Ce **(b)** Ce-CA **(c)** Ce-CTAB **(d)** Ce-Com.

The bandgap of all the samples was calculated from the reflectance spectra using the Kubelka-Munk function and Tauc's plot. The bandgap was found to lie between 2.8 eV and 2.9 eV (Figure 8); hence, the synthesized nanostructures were defined to be purely semiconductor by nature. Intrinsic defects, such as oxygen vacancies and Ce^{3+}/Ce^{4+} redox pairs, caused the variations in the bandgap by influencing the electronic structure of CeO_2 NPs (24). However, the *Ce-com* showed a bandgap of 3.1 eV, consistent with the reported bandgap of bulk CeO_2 (25). Compared to the bulk value, this reduced bandgap suggested that the synthesized NPs could function as suitable catalysts for photochemical reactions (26). Huang et al. reported a range of bandgaps from 3.42 eV to 2.94 eV with increasing particle size, and discussed the relationship between bandgap and particle size of the nanoparticles (27).

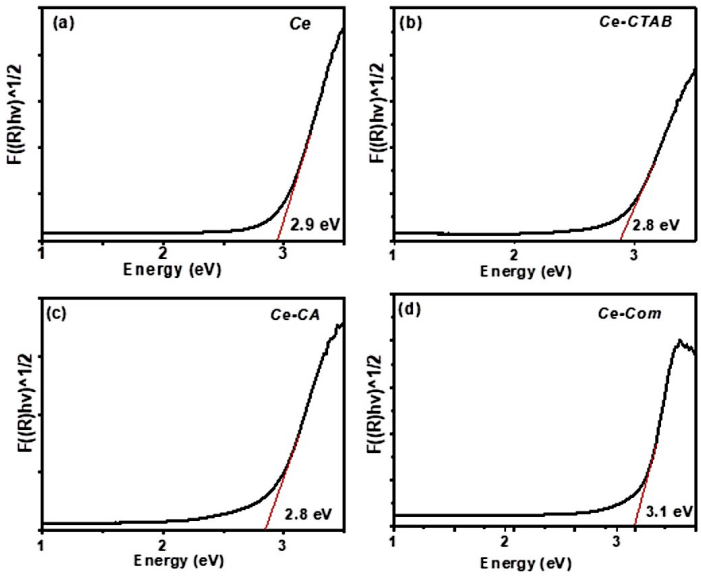

Figure 8. Graphical representation of bandgap of CeO_2 nanostructures **(a)** Ce **(b)** Ce-CTAB **(c)** Ce-CA **(d)** Ce-Com.

In all the synthesized CeO_2 NPs, a broad band ~ 3384 cm^{-1} corresponding to the stretching of –OH associated with the surface hydroxyl groups from water molecules was observed. The functionalized CeO_2 samples showed vibrations corresponding to the functional group attached to the CeO_2 NPs. In these materials, we observed bands ~ 497 cm^{-1} and 676 cm^{-1}, which correspond to the Ce-O stretching vibration of the IR active F_{1U} mode of the fluorite structure. Two intense bands due to -C-O and COO^- were present at 1549 cm^{-1} and 1454 cm^{-1} due to the absorbed carbonate molecules. Additionally, the C–H stretching vibrations observed at 2929 cm^{-1} and 2849 cm^{-1} were attributed to the alkyl chains of the capping agents used during functionalization. The commercial CeO_2 showed intense bands at ~ 726 cm^{-1} and 512 cm^{-1}, indicative of the stretching vibrations of the Ce–O bond (28).

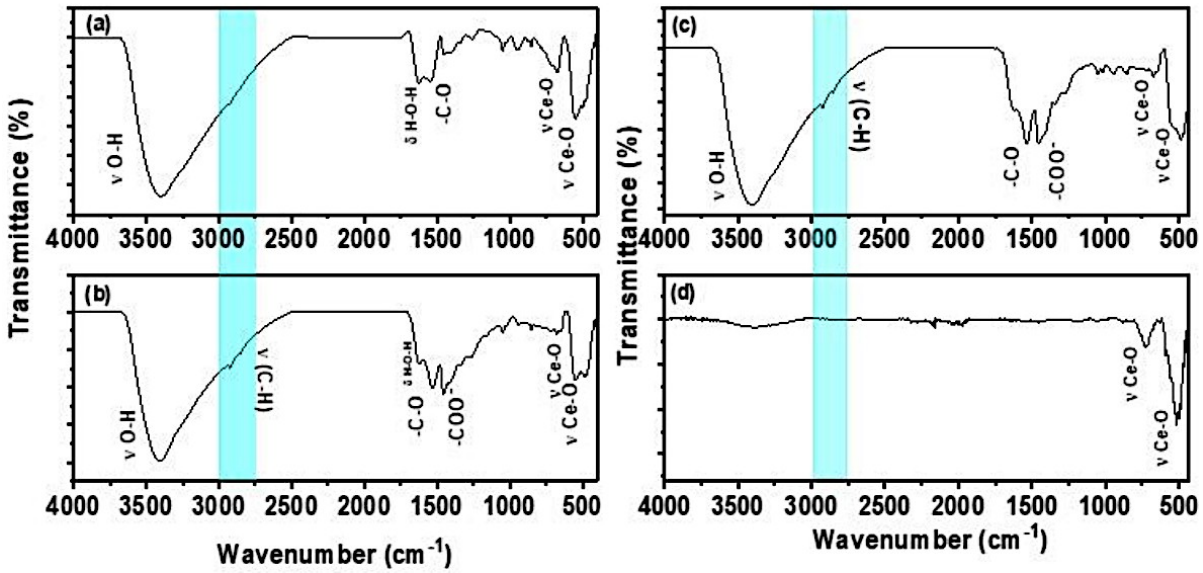

Figure 9. FTIR spectra of **(a)** Ce **(b)** Ce-CA **(c)** Ce-CTAB **(d)** Ce-Com.

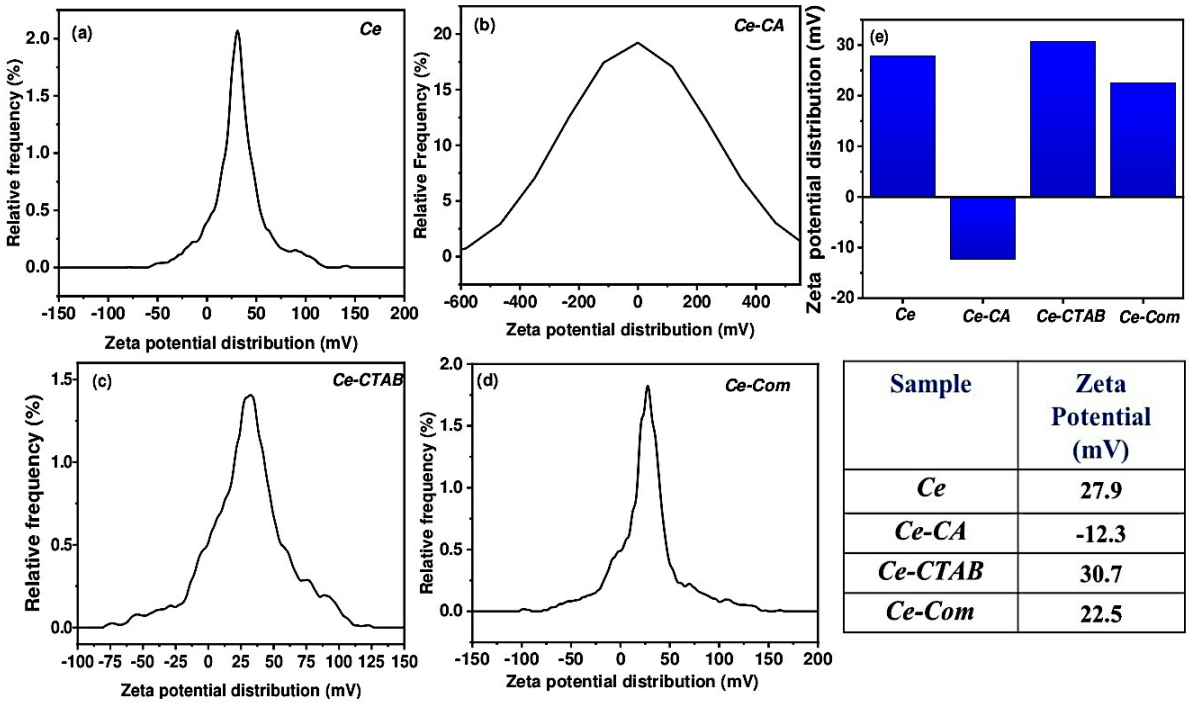

Sample	Zeta Potential (mV)
Ce	27.9
Ce-CA	-12.3
Ce-CTAB	30.7
Ce-Com	22.5

Figure 10. Zeta potential analysis of **(a)** Ce **(b)** Ce-CA **(c)** Ce-CTAB **(d)** Ce-Com **(e)** Bar diagram showing the zeta potential distribution.

Figure 10 shows the zeta potential of the nanoparticles. We prepared an aqueous dispersion of each nanoparticle sample in Type 1 water at a concentration of 1 mg/mL for the measurements. The experiments were performed under ambient conditions to

determine the nature of NP surface charges (29). The *Ce* nanoparticles' zeta potential was found to be +27.9 mV, indicating a positively charged surface at neutral pH. In contrast, the *Ce-CA* sample exhibited a zeta potential of -12.3 mV. *Ce-CTAB* showed a higher positive value of +30.7 mV, suggesting strong surface charge contributions from the stabilizing agents. The negative zeta potential of *Ce-CA* was attributed to the anionic nature of citric acid, whereas the positive charge of *Ce-CTAB* was attribuuted to the cationic surfactant CTAB (30). The commercial Ce sample (*Ce-Com*) displayed a zeta potential of +22.5 mV, further supporting the influence of surface modifications on colloidal stability.

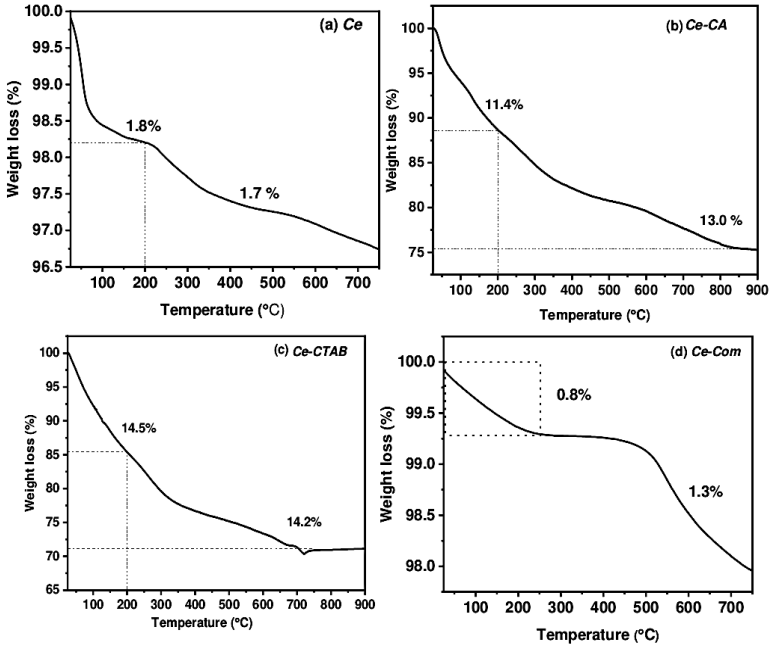

Figure 11. Thermogravimetric analysis of **(a)** Ce **(b)** Ce-CA **(c)** Ce-CTAB **(d)** Ce-Com.

TGA was performed by heating the samples from room temperature to 900 °C at 10 °C per minute. The sample lost weight between 100 °C and 200 °C due to the removal of surface water molecules (31), and between 200 °C and 600 °C due to the decomposition of organic compounds (32). CeO_2 exhibits high thermal stability, with a melting point of ~ 2500 °C (33). The initial weight loss in the samples was observed as 1.8%, 11.4%, 14.5%, and 0.8% for Ce, *Ce-CA, Ce-CTAB,* and *Ce-Com*, respectively, at temperatures between 100 -200°C, attributed to the loss of surface water molecules.

The Ce sample showed a loss of 1.7% between 200°C and 700°C due to the loss of organic compounds (34). The *Ce-CA* showed a loss of 13.0% at 200°C to 750°C due to the loss of organic compounds, i.e., citric acid. For the *Ce-CTAB* sample, there was a 14.2% loss due to the loss of organic compounds, i.e, CTAB. The *Ce- Com* sample showed a loss of 1.3% at 500°C, which could be due to the organic impurities present in the sample.

Further, the final weights were 96.5%, 75.6%, 71.3%, and 97.9% for *Ce, Ce-CA, Ce-CTAB,* and *Ce-Com,* respectively. The

TGA data, taken along with the dialysis experiment to remove non-adsorbed capping agents, thus suggest that the capping agents are chemisorbed on the CeO_2 NPs.

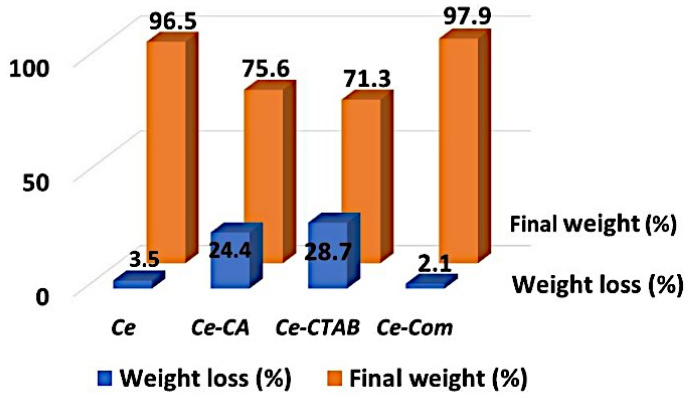

Sl. No	Sample	Weight loss (%)	Final weight (%)
1	*Ce*	3.5	96.5
2	*Ce-CA*	24.4	75.6
3	*Ce-CTAB*	*28.7*	71.3
4	*Ce-Com*	2.1	97.9

Figure 12. Bar diagram representing TGA analysis of various samples.

The d-values (interplanar spacings) were calculated from the XRD 2θ peaks at https://instananо.com/all/characterization/xrd/d-value/ and a wavelength of 1.5406 A°. These were found to be equal to the those presented in Figures 4 through 6 for the (h, k and l) Miller indices. The lattice parameter, a, was then calculated using the equation $a^2=\frac{h^2+l^2+k^2}{d^2}$ to be 5.39 A° using any of the three Miller indices of (1,1,1), (2,0,0) or (2,2,0). The molecules of capping agent per nm^2 of surface area of an NP, A, were calculated using the equation,

$$A=\frac{fracW*\rho*r*N}{3*Mw*\left[1-\left(fracW\right)\right]},$$

where fracW=Fractional Weight loss (percent weight loss/100), ρ=density of the core NP (~ to that of CeO_2) taken to be 7.22 g/cm^3, r=radius of the NP in nm, N=Avagadro's number (molecules/mole) and Mw=molar mass of capping agent (g/mole). The molar masses of citric acid and CTAB were 192.1 and 364.5 g/mole respectively. The radii of the Ce-CA Nps and Ce-CTAB NPs were 3.5 nm and 3.0 nm from Figures 5 and 6 respectively. Table 3 shows the calculated molar (molecule) ratio of the capping agent to the CeO_2 molecules at the surface of each NP.

Table 3. Calculated mole ratio for capping agent to CeO_2 at the surface of NP

	A (molecules of capping agent per nm^2 of surface area of NP	Surface area of NP (nm^2)	# of molecules of capping agent per NP	# of CeO_2 molecules at the surface of each NP*	# of CeO_2 surface molecules for every molecule of capping agent
Citric acid	3.95	153.9	608	2855	4.7
CTAB	1.97	113	223	2096	9.4

*Calculated as Surface area of NP in A° divided by the lattice parameter 5.39 A°

The results from Table 3 imply that there is 1 molecule of citric acid functionalized for every ~ 5 CeO_2 NP surface molecules and there is 1 molecule of CTAB functionalized for every 9 CeO_2 NP surface molecules. Therefore, the functionalization of any of the capping agents is not enough for complete engagement of the CeO_2 NP surface molecules as shown in Figure 13 (a, b). The percent molar saturation is calculated as 3/5=60% for Citric acid and 78% for CTAB. It could be that stearic hindrance prevents 100% saturation of capping agents on the surface. However, further experimentation needs to be performed with a greater stoichiometric ratio of capping agents to CeO_2, or a change in the synthesis conditions to confirm.

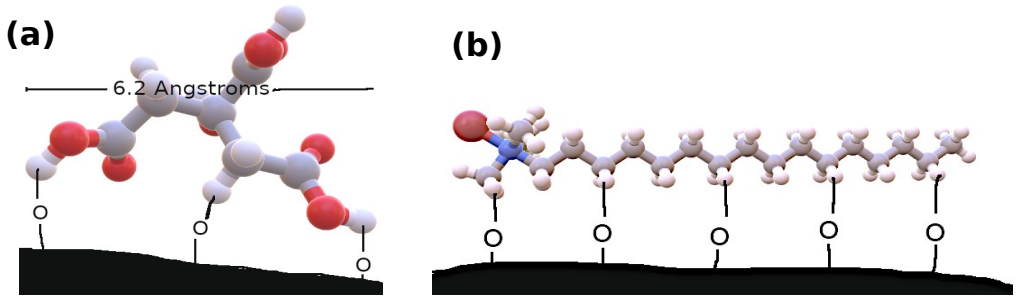

Figure 13. (a) Left panel. A maximum of 3 molecules of CeO_2 can interact with the -H atoms of the Citric acid, due to an interplanar distance of 2.7 A^o for the former. **(b)** A maximum of 7 molecules (5 shown in the figure) of CeO_2 can interact with the -H atoms of the CTAB, due to an interplanar distance of 1.9 A^o for the former. The C-H bond length is 1.54 A^o . Not shown is the overall electrovalent attraction of the carboxyl group(s) of the citric acid to the Ce^{+3}/Ce^{+4} charged atoms of the CeO_2, which also undoubtedly contributes to functionalization.

It also remains to be seen whether hydrophobicity imparted by Citric acid or CTAB can be increased further with greater potential surface molar coverage of these capping agents.

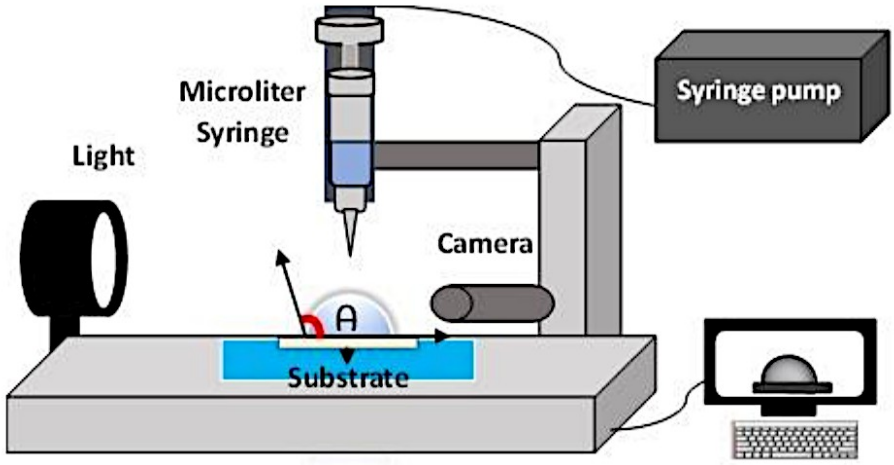

Figure 14. Schematic diagram of the experimental setup of the contact angle meter.

The study also examined the wetting properties of the nanostructures using a contact angle meter, employing the sessile drop method for contact angle measurement. We placed a sessile drop at each position and took measurements at five different positions on the substrate. The volume of water used was one µL per sample. Figure 14 shows a schematic diagram of the experimental setup of the contact angle meter.

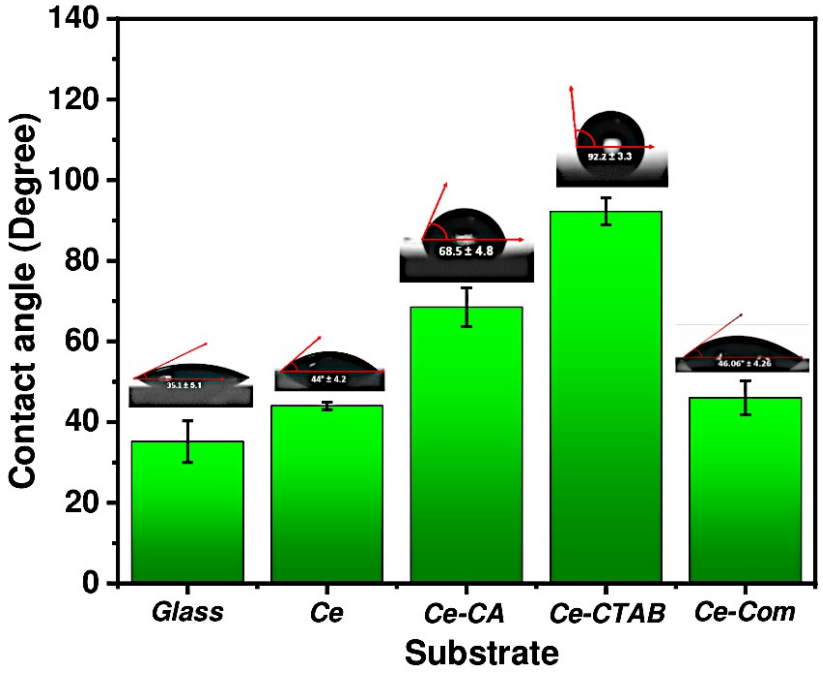

Figure 15. Contact angles of various substrates.

Figure 15 shows the contact angle of various substrates. The contact angle measurements show that the glass substrate exhibited hydrophilic behavior, with a contact angle of 35.1° ± 5.1°. The unfunctionalized *Ce* showed a greater contact angle of 44.2° ± 4.2°, indicating a modest increase in hydrophobicity compared to the glass substrate. However, with the introduction of citric acid as a capping agent during synthesis, the contact angle significantly increased to 68.5° ± 4.8°. This may be because the hydrophilic influence of the unbound carboxylic and hydroxyl functional groups on the citric acid molecule is more than offset by the 'masking' or stearic hindrance to the -O atoms of the surface CeO_2 by the citric acid (which would otherwise have formed -H bonds with H_2O). Even though the -H atoms from H_2O may find a way in between the citric acid molecule and the NP surface, in this case the larger loss in entropy may offset the negative enthalpic contribution from forming an -H bond with the 'masked' -O atoms of the CeO_2. The orientation of CA molecules on the CeO_2 surface is hence causative in the observed increase in contact angle after citric acid functionalization. Here, the carboxylate ($–COO^-$) groups of CA chelate strongly with Ce^{3+}/Ce^{4+} sites on the nanoparticle surface, causing the hydrophobic hydrocarbon chains ($–CH_2$) to face outward toward the water interface. Although FTIR data cannot suport this hypothesis directly, the presence of $–CH_2$ groups on the functionalized surface was

confirmed by strong C-H stretching vibrations in th e 2850-3000 cm^{-1} region. Although carboxylates are inherently hydrophilic, their binding geometry dictates wettability. In our configuration, chelation folds the $–COO^–$ groups toward CeO_2 rather than the water phase, while the exposed $–CH_2$ groups dominate the interfacial energetics, thereby increasing hydrophobicity. The observed increase in contact angle upon citric acid (CA) functionalization is consistent with prior studies on Ce-based films, such as Marunkicl et al., who reported that Ce-citrate films on AISI 4130 steel yielded water contact angles of 50–65° (vs. 35–40° for Ce-chloride), with prolonged immersion further increasing contact angle to ~71.7° after 96 h, thus demonstrating surface functionalization's critical role in modulating nanomaterials' wettability. This trend was attributed to the formation of a denser, more compact inhibitory film in Ce-citrate systems, likely due to the chelating action of citrate (35).

Remarkably, CeO_2 nanoparticles functionalized with CTAB exhibited a contact angle of 92.2° ± 3.3° within the hydrophobic regime. This substantial increase in hydrophobicity is due to the intrinsic properties of CTAB, a cationic surfactant with a 16-carbon alkyl chain. The long hydrocarbon chain of CTAB introduces a high density of non-polar C-H bonds on the nanoparticle surface, thereby increasing surface energy and enhancing hydrophobicity (36,37). The hydrophobic nature of CTAB-functionalized CeO_2 nanoparticles was further supported by the principle that non-polar molecules, such as hydrocarbons, minimize interactions with polar solvents like water, leading to higher contact angles. The commercial CeO_2 exhibited a contact angle of 46.1°±4.2°, depicting the importance of functionalisation with a capping agent. Table 4 shows the contact angle for various substrates.

Table 4. Comparative analysis of the impact of capping agents on the physicochemical properties of CeO_2 NPs

Sample	Capping agent	Morphology	Particle size, (nm)	Band gap (eV)	Crystallinity	CH_2 groups from FTIR	Zeta potential (mV)	Contact angle (Degrees)
Ce	Not added	Irregular polygons with sharp edges	9	2.9	Polycrystalline	Not appreciable	27.9	44.2° ± 4.2°
Ce- CA	Citric acid	Irregular polygons & spheres	7	2.8	Polycrystalline	Present evidently	-12.3	68.5° ± 4.8°
Ce-CTAB	Cetrimonium bromide	Irregular polygons & spheres	6	2.8	Polycrystalline	Present evidently	30.7	92.2° ± 3.3°
Ce- comm	Not added	Irregular shapes	88	3.1	Crystalline	Not present	22.5	46.06°±4.2°
glass	-	-	-	-	-	-	-	35.1°±5.1°

These results show the influence of surface functionalization on the wettability of nanomaterials, with CTAB proving particularly effective in imparting hydrophobic characteristics. This behavior is consistent with previous studies on surfactant-mediated surface modifications, where the introduction of long alkyl chains significantly enhanced hydrophobicity (16). Such tailored wettability is crucial for applications in self-cleaning surfaces, water-repellent coatings, and selective catalysis, where control over surface interactions is essential.

Conclusion

In this study, we successfully synthesized CeO_2 NPs using a facile hydrothermal method, with citric acid (CA) and cetrimonium bromide (CTAB) as capping agents to control their morphology and surface properties. XRD, Raman spectroscopy, FESEM, TEM, and FTIR characterized the synthesized nanoparticles, confirming their cubic crystal structure, high crystallinity, morphology, and functionalization. The results demonstrated that the choice of capping agent significantly influenced the nanoparticles' size, morphology, and wettability. Citric acid reduced the particle size to ~7 nm, while CTAB further decreased it to ~6 nm, highlighting the role of capping agents in modulating nanoparticle growth and aggregation.

Using data from the dialysis, XRPD and TGA experiments, it was calculated that the surface molar saturation of CeO_2 molecules was 66% when functionalized with citric acid and 77% when functionalized with CTAB; i.e. less than that for a complete monolayer coverage. Such calculations are useful for correlating NP properties such as morphology and hydrophobicity with molar functionalization.

The wettability studies found that surface functionalization played a critical role in tailoring the hydrophobicity of CeO_2 NPs. Unfunctionalized CeO_2 exhibited a modest contact angle of 44.2° ± 4.2°, while citric acid-functionalized nanoparticles showed an increased contact angle of 68.5° ± 4.8°. Remarkably, CTAB-functionalized CeO_2 NPs achieved a contact angle of 92.2° ± 3.3°, demonstrating significant hydrophobicity. The long alkyl chains of CTAB on the surface of the NPs increased the interfacial free energy and minimized interactions with polar solvents, leading to this contact angle increase. These findings provide valuable insights into the relationship between synthesis parameters, surface functionalization, and the wettability of CeO_2 nanoparticles. The ability to control hydrophobicity through surface modification opens new avenues for applications. This work shows the importance of capping agents in designing nanomaterials with tailored properties for specific technological applications. Future studies could explore the scalability of this synthesis method and investigate the performance of these functionalized nanoparticles in environmental remediation, energy storage, and biomedical applications.

Acknowledgments

The authors acknowledge Prayoga Institute of Education Research, Bengaluru, and CRF at CeNS for the characterization facility. The authors acknowledge Dr. Bramhaiah Kommula for helpful technical discussions.

References

1. Qiao, L., Swihart, M. T. (2017). Solution-phase synthesis of transition metal oxide nanocrystals: Morphologies, formulae, and mechanisms. Advances in Colloid and Interface Science, 244, 199-266. http://dx.doi.org/10.1016/j.cis.2016.01.005

2. Singh, K. K., Prabhu, R.B., Ramakrishnan, V., John, N. S. (2017). Rapid augmentation of vertically aligned MoO_3 nanorods via microwave irradiation. CrystEngComm, 19(44), 6568-6572. https://doi.org/10.1039/C7CE01531C

3. Song, H. W., Kim, N. Y., Park, J. E., Ko, J. H., Hickey, R. J., Kim, Y. H., Park, S. J. (2017). Shape-controlled syntheses of metal oxide nanoparticles by the introduction of rare-earth metals. Nanoscale, 9(8), 2732-2738. https://doi.org/10.1039/C6NR07555J

4. Preisler, E. J. (2003). Investigation of novel semiconductor heterostructure systems: I. Cerium oxide/silicon heterostructures II. 6.1 Å semiconductor-based avalanche photodiodes. California Institute of Technology.

5. Chen, B. H., Stephen Inbaraj, B. (2018). Various physicochemical and surface properties controlling the bioactivity of cerium oxide nanoparticles. Critical reviews in biotechnology, 38(7), 1003-1024. https://doi.org/10.1080/07388551.2018.1426555

6. Jiang, Y., Fu, H., Liang, Z., Zhang, Q., Du, Y. (2024). Rare earth oxide based electrocatalysts: synthesis, properties and applications. Chemical Society Reviews, 53(2), 714-763. https://doi.org/10.1039/D3CS00708A.

7. Nag, S., Mitra, O., Bhattacharjee, A., Mohanto, S., Gowda, B. J., Kar, S., et al. (2024). Exploring the emerging trends in the synthesis and theranostic paradigms of cerium oxide nanoparticles (CeONPs): A comprehensive review. Materials Today Chemistry, 35, 101894. https://doi.org/10.1016/j.mtchem.2023.101894

8. Lin, M., Fu, Z.Y., Tan, H.R., Tan, J.P.Y., Ng, S.C., Teo, E. (2012). Hydrothermal synthesis of CeO_2 nanocrystals: Ostwald ripening or oriented attachment?. Crystal growth & design, 12(6), 3296-3303. https://doi.org/10.1021/cg300421x

9. An, K., Wang, Y., Sui, Y., Qing, Y., Tong, W., Wang, X., Liu, C. (2025). Recent advances of cerium compounds in functional coatings: Principle, strategies and applications. Journal of Rare Earths, 43(2), 227-245. https://doi.org/10.1016/j.jre.2024.03.017.

10. Atran, A. A., Ibrahim, F. A., Hamdy, M. S. (2024). Functionalization and applications of the versatile CeO_2 nanoparticles: A review. Inorganic Chemistry Communications, 163, 112359. https://doi.org/10.1016/j.inoche.2024.112359.

11. Guo, F., Guo, Z. (2016). Inspired smart materials with external stimuli responsive wettability: a review. Rsc Advances, 6(43), 36623-36641. https://doi.org/10.1039/C6RA04079A.

12. Jayaramulu, K., Geyer, F., Schneemann, A., Kment, Š., Otyepka, M., Zboril, R., et al. (2019). Hydrophobic metal–organic frameworks. Advanced Materials, 31(32), 1900820. https://doi.org/10.1002/adma.201900820.

13. Mai, H. X., Sun, L. D., Zhang, Y. W., Si, R., Feng, W., Zhang, H. P., et al. (2005). Shape-selective synthesis and oxygen storage behavior of ceria nanopolyhedra, nanorods, and nanocubes. The Journal of Physical Chemistry B, 109(51), 24380-24385. https://doi.org/10.1021/jp055584b.

14. Li, X. P., Sun, Y. L., Xu, Y. Y., Chao, Z. S. (2018). UV-Resistant and Thermally Stable Superhydrophobic CeO_2 Nanotubes with High Water Adhesion. Small, 14(27), 1801040. https://doi.org/10.1002/smll.201801040.

15. Azimi, G., Dhiman, R., Kwon, H. M., Paxson, A. T., Varanasi, K. K. (2013). Hydrophobicity of rare-earth oxide ceramics. Nature materials, 12(4), 315-320. https://doi.org/10.1038/nmat3545.

16. Sanders, S., Golden, T. D. (2019). Functionalization of cerium oxide nanoparticles to influence hydrophobic properties. Langmuir, 35(17), 5841-5847. https://doi.org/10.1021/acs.langmuir.9b00201.

17. Calvache-Muñoz, J., Prado, F. A., Rodríguez-Páez, J. E. (2017). Cerium oxide nanoparticles: Synthesis, characterization and tentative mechanism of particle formation. Colloids and Surfaces A: Physicochemical and Engineering Aspects, 529, 146-159. https://doi.org/10.1016/j.colsurfa.2017.05.059.

18. Yogamalar, R., Srinivasan, R., Vinu, A., Ariga, K., Bose, A. C. (2009). X-ray peak broadening analysis in ZnO nanoparticles. Solid State Communications, 149(43-44), 1919-1923. https://doi.org/10.1016/j.ssc.2009.07.043.

19. De Sousa, M. E., Fernandez van Raap, M. B., Rivas, P. C., Mendoza Zélis, P., Girardin, P., Pasquevich, G. A., Sánchez, F. H. (2013). Stability and relaxation mechanisms of citric acid coated magnetite nanoparticles for magnetic hyperthermia. The Journal of Physical Chemistry C, 117(10), 5436-5445. https://doi.org/10.1021/jp311556b.

20. Lu, A. H., Salabas, E. E., Schüth, F. (2007). Magnetic nanoparticles: synthesis, protection, functionalization, and application. Angewandte chemie international edition, 46(8), 1222-1244. https://doi.org/10.1002/anie.200602866.

21. Sun, C., Li, H., Wang, Z., Chen, L., Huang, X. (2004). Synthesis and characterization of polycrystalline CeO_2 nanowires. Chemistry Letters, 33(6), 662-663. https://doi.org/10.1246/cl.2004.662.

22. Balakrishnan, G., Raghavan, C. M., Ghosh, C., Divakar, R., Mohandas, E., Song, J. I., Kim, T. G. (2013). X-ray diffraction, Raman, and photoluminescence studies of nanocrystalline cerium oxide thin films. Ceramics International, 39(7), 8327-8333. http://dx.doi.org/10.1016/j.ceramint.2013.03.103.

23. Loridant, S. (2021). Raman spectroscopy as a powerful tool to characterize ceria-based catalysts. Catalysis Today, 373, 98-111. https://doi.org/10.1016/j.cattod.2020.03.044.

24. Bazhukova, I. N., Sokovnin, S. Y., Ilves, V. G., Myshkina, A. V., Vazirov, R. A., Pizurova, N., Kasyanova, V. V. (2019). Luminescence and optical properties of cerium oxide nanoparticles. Optical Materials, 92, 136-142. https://doi.org/10.1016/j.optmat.2019.04.021.

25. Thill, A. S., Lobato, F. O., Vaz, M. O., Fernandes, W. P., Carvalho, V. E., Soares, E. A., et al. (2020). Shifting the band gap from UV to visible region in cerium oxide nanoparticles. Applied Surface Science, 528, 146860. https://doi.org/10.1016/j.apsusc.2020.146860.

26. Zhang, C., Ahmad, I., Ahmed, S.B., Ali, M.D., Karim, M.R., Bayahia, H. and Khasawneh, M.A. (2024). A review of rare earth oxides-based photocatalysts: Design strategies and mechanisms. Journal of Water Process Engineering, 63, 105548. https://doi.org/10.1016/j.jwpe.2024.105548.

27. Huang, Y. C., Wu, S. H., Hsiao, C. H., Lee, A. T., Huang, M. H. (2020). Mild synthesis of size-tunable CeO2 octahedra for band gap variation. Chemistry of Materials, 32(6), 2631-2638. https://doi.org/10.1021/acs.chemmater.0c00318.

28. Safat, S., Buazar, F., Albukhaty, S., Matroodi, S. (2021). Enhanced sunlight photocatalytic activity and biosafety of marine-driven synthesized cerium oxide nanoparticles. Scientific Reports, 11(1), 14734. https://doi.org/10.1038/s41598-021-94327-w.

29. Singh, R. P., Sharma, K., Mausam, K. (2020). Dispersion and stability of metal oxide nanoparticles in aqueous suspension: A review. Materials Today: Proceedings, 26, 2021-2025. https://doi.org/10.1016/j.matpr.2020.02.439.

30. Habib, I. Y., Kumara, N. T. R. N., Lim, C. M., Mahadi, A. H. (2018). Dynamic light scattering and zeta potential studies of ceria nanoparticles. Solid State Phenomena, 278, 112-120. https://doi.org/10.4028/www.scientific.net/SSP.278.112.

31. Hancock, M. L., Yokel, R. A., Beck, M. J., Calahan, J. L., Jarrells, T. W., Munson, E. J., et al. (2021). The characterization of purified citrate-coated cerium oxide nanoparticles prepared

via hydrothermal synthesis. Applied Surface Science, 535, 147681. https://doi.org/10.1016/j.apsusc.2020.147681.

32. Kommula, B., Prabhu B, R., Kopperi, H., Bhat, V. S., Hegde, G., John, N. S. (2024). Diverse Morphologies of Nb_2O_5 Nanomaterials: A Comparative Study for the Growth Optimization of Elongated Spiky Nb_2O_5 and Carbon Nanosphere Composite. Particle & Particle Systems Characterization, 41(3), 2300118. https://doi.org/10.1002/ppsc.202300118.

33. Aristova, N. M. (2022). Thermodynamic properties of cerium dioxide in the condensed state. High Temperature, 60(6), 756-760. https://doi.org/10.1134/S0018151X22040095.

34. Chaudhary, S., Sharma, P., Kumar, R., Mehta, S. K. (2015). Nanoscale surface designing of Cerium oxide nanoparticles for controlling growth, stability, optical, and thermal properties. Ceramics International, 41(9), 10995-11003. http://dx.doi.org/10.1016/j.ceramint.2015.05.044.

35. Marunkić, D., Jegdić, B., Pejić, J., Milošević, M., Marinković, A., Radojković, B. (2022). Analysis of inhibitory properties of Ce-citrate as a green corrosion inhibitor of low alloy steel in neutral chloride solution. Materials and Corrosion, 73(8), 1286-1297. https://doi.org/10.1002/maco.202213079.

36. Qiu, P., Jensen, C., Charity, N., Towner, R., Mao, C. (2010). Oil phase evaporation-induced self-assembly of hydrophobic nanoparticles into spherical clusters with controlled surface chemistry in an oil-in-water dispersion and comparison of behaviors of individual and clustered iron oxide nanoparticles. Journal of the American Chemical Society, 132(50), 17724-17732. https://doi.org/10.1021/ja102138a.

37. Li, R., Wang, Z., Gu, X., Chen, C., Zhang, Y., Hu, D. (2020). Study on the assembly structure variation of cetyltrimethylammonium bromide on the surface of gold nanoparticles. ACS omega, 5(10), 4943-4952. https://doi.org/10.1021/acsomega.9b03823.